# Simulation of vortical flow over a slender delta wing experiencing vortex breakdown

B.I. Soemarwoto and O.J. Boelens

NLR-TP-2003-396

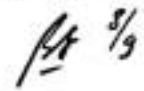# Simulation of vortical flow over a slender delta wing experiencing vortex breakdown

B.I. Soemarwoto and O.J. Boelens

| Approved by author: | Approved by project manager: | Approved by project managing department: |
|---|---|---|
| /M 8/9 | 8/9 | C 9/9/2003 |

## Summary

This paper presents an application of CFD methodology based on the unsteady Reynolds-Averaged Navier-Stokes (RANS) equations with a $k - \omega$ turbulence model for the prediction of vortical flows involving vortex breakdown. A variant of the $k$-$\omega$ turbulence model is applied that avoids excessively high eddy viscosity in the vortex cores. Time-accurate simulations are performed for subsonic flow around the ONERA 70 degree delta wing at an angle of attack of 27 degrees. Two non-dimensional time steps of different order of magnitude, are used. Both simulations predict vortex breakdown. The smaller time step leads to a self-sustained oscillation. Computational results are compared with the experimental data, and discussed in terms of pressure coefficient, velocity and vorticity components, and turbulence kinetic energy distributions on the crossflow planes and on the longitudinal plane along the vortex core. A Fourier analysis results in a spectrum with a distinct frequency peak of the Strouhal number approximately equal to 9.

# Contents

16 Figures

(27 pages in total)

## Nomenclature

| | |
|---|---|
| $C_p$ | pressure coefficient |
| $C_f$ | skin friction coefficient |
| $c$ | wing root chord |
| $f$ | frequency (Hz) |
| $k$ | Turbulence kinetic energy |
| $r$ | vortex core sensor |
| St | Strouhal number |
| $u$ | $x$-component of the velocity |
| $v$ | $y$-component of the velocity |
| $w$ | $z$-component of the velocity |
| $x, y, z$ | axes of the Cartesian coordinate system |
| $U_o$ | magnitude of the free-stream velocity |
| $\alpha$ | angle of attack |
| $\eta$ | local non-dimensional spanwise coordinate |

This page is intentionally left blank.

# 1 Introduction

Leading edge vortices are dominant phenomena in the flow around modern high performance fighter aircraft. While vortices are advantageous in augmenting lift by creating high suction fields above the wing, the phenomenon called vortex breakdown can lead to severe problems. Unsteady vortex breakdown raises serious aeroelastic concerns due to problems such as buffetting, especially for aircraft with twin vertical tails. Ventral fins immersed in a bursted vortex field experience buffet loads that may lead to early structural problems related to fatigue. Flow unsteadiness caused by vortex breakdown also affects the flutter speed and the magnitude of limit cycle oscillations.

From the performance point of view, leading edge vortices are instrumental for maneuvering in high angle-of-attack regimes. The onset of vortex breakdown, however, determines the maximum vortex-induced lift that can be attained during such maneuvers. Vortex breakdown initiates a process that reverses the angle-of-attack trends of the force and moment coefficients. Stability and control issues follow, as asymmetric vortex breakdown over the wing potentially initiates roll instabilities which can lead to departure from controlled flight, and drastic trend reversal in the longitudinal and lateral stability derivatives reduce the control authority. For aircraft with twin vertical tails, a bursted vortex impinging on a vertical fin deteriorates the effectiveness of the rudder.

A good understanding of the susceptibility to departure, the departure motion itself, and an accurate assessment of agility potential of modern high performance aircraft are critical to flight safety for which the risk of losing aircraft and/or pilot in combat situation must be minimized (Ref. 1). A challenging task is to estimate departure boundaries (Refs. 2, 10) accurately by means of simulations based on Computational Fluid Dynamics (CFD). This task is particularly relevant as modern fighter aircraft design allows penetration into extreme flow conditions characterized by high angles of attack and high angular rates. CFD methods account for strong non-linearities involved in such extreme flow conditions, and facilitate the evaluation of departure criteria in terms of stability and control derivatives covering non-linear flow regimes (Refs. 14, 5). A thorough assessment of the stability and control properties, however, can be obtained by complete simulation of the aircraft motion through coupling CFD methods and Flight Mechanics methods.

Both the advantages and the risks involved with leading edge vortices in high angle-of-attack flow regimes have motivated numerous experimental, theoretical and numerical investigations. Within the task group RTO-AVT080 *Vortex Breakdown over Slender Wings* an opportunity is provided to assess CFD capability to calculate vortical flow experiencing vortex breakdown on the basis of available experimental data (Refs. 11, 12). Accurate simulation of vortical flows experiencing

vortex breakdown is important, because the captured characteristics of the breakdown determines in a global way the pressure distribution over the wing surface and, thus, the aerodynamic force and moment coefficients.

This paper presents an application of CFD methodology based on the unsteady Reynolds-Averaged Navier-Stokes (RANS) equations for the prediction of vortical flow involving vortex breakdown. Modelling based on RANS equations assumes a clear separation of the time scales of the vortex breakdown and the turbulence unsteadiness. The present choice for the RANS method has been made under constraints of the available computational resource, whilst a RANS simulation provides results that can be contrasted with those to be obtained using a higher fidelity modelling given by a hybrid RANS/LES method (Ref. 7).

A variant of the $k$-$\omega$ turbulence model is applied that avoids excessively high eddy viscosity in the vortex cores. Time-accurate simulations are performed for subsonic flow around the ONERA 70 degree delta wing at an angle of attack of 27 degrees. Computational results are compared with the experimental data.

## 2   Flow modelling

Subsonic flow around a half-span configuration of the ONERA 70 degree delta wing with sting (Ref. 11) is considered. The delta wing has a flat surface on the leeward side where the leading edge vortices occur. The wing root chord is 950 mm. The unsteady Reynolds-Averaged Navier-Stokes (RANS) equations are employed in a flow domain discretized by structured grids. The flow domain around the wing/sting configuration is divided into 50 blocks of structured grids. Figure 1 gives an impression of the flow domain topology in the near-field and the structured grids on the wing surface, a crossflow plane and the symmetry plane. In total, the flow domain around the half-span configuration contains 3,694,080 grid cells, with 160 cells along the wing chord and 144 cells along the wing span over the upper surface.

A calorically perfect gas relation, the Stokes' hypothesis for a Newtonian fluid, and the Sutherland's law for the dynamic molecular viscosity are assumed to hold throughout the flow field. The Boussinesq assumption is used for the formulation of the Reynolds stress tensor using the concept of eddy viscosity.

No-slip and adiabatic wall boundary conditions are applied on the solid surfaces. In the experiment, a transition trip is applied at 40% chord aft of the wing apex. However, during the simulation turbulent flow over the wing surface is enforced, allowing non-zero eddy viscosity in the vortex. The reason for this treatment is that the interfaces separating the regions of the boundary layer, the vortices, and the shear layers emanating from the leading edge, cannot be exactly identified, so that a proper zonal modelling cannot be arranged. In addition, it is considered that while the boundary layer may be laminar upstream of the transition trip, it is not clear whether the leading edge vortex and the shear layers are also laminar, as turbulence may already be generated in the shear layers and fed into the vortex.

For the determination of the turbulence kinetic energy and the eddy viscosity, a variant of the Wilcox $k$-$\omega$ turbulence model is applied, with the free-stream dependency and the singular behaviour near solid walls resolved (Refs. 6, 8). The turbulence-model equations and the mean flow (RANS) equations are solved simultaneously for the mean flow variables using NLR's CFD system ENFLOW (Ref. 3). The spatial discretization employs a cell-centered finite volume scheme. For the mean flow equations, Jameson-type artificial dissipation fluxes are added consisting of blended first and third order differences with a pressure-based shock sensor. The artificial dissipation terms are implemented with matrix coefficients to enhance the accuracy . For the turbulence-model equations, artificial diffusive fluxes are also defined using blended first and third order differences, with the scaling factor given by the eigenvalue of the convective flux in the turbulence equations.

It is well known that standard RANS methods produce high levels of eddy viscosity in the vortex core giving excessive dissipation. For these methods, the details of the vortex core are lost and low suction peaks with wide vortex bases are a characteristic of the solution. As a remedy, a modification to the $k$-$\omega$ turbulence model is applied. A parameter $r$ is used to detect vortex cores. This parameter is the ratio between the magnitude of strain-rate and vorticity tensor. In shear layers, the velocity gradient is dominated by the gradient in the normal direction, which gives $r \approx 1$, while in vortex cores $r \ll 1$ where the flow experiences pure rotation. Based on this parameter the production of turbulence kinetic energy is limited in vortex cores through a promoted production of the dissipation rate. This approach has proven to be effective in producing suction peak profiles in good agreement with those of experimental data (Refs. 4, 15).

For time-accurate simulations, a second-order dual-time stepping scheme is applied, using a five-stage explicit Runge-Kutta scheme for each physical time step and acceleration techniques such as local-time stepping, implicit residual averaging and multi-grid. The source terms in the turbulence equations are treated explicitly using a separate time-step for efficiency.

## 3  Results

The subsonic flow around the delta wing is defined by a Mach number $M = 0.069$, an angle of attack $\alpha = 27$ degrees, and a Reynolds number Re $= 1.56$ millions. As a low Mach number is involved, global low-Mach preconditioning was applied (Ref. 9) to the system of equations during the simulation. The free-stream velocity $U_o$ is 24 m/s. As a first test, a steady simulation was performed using the free-stream velocity as an initial solution. The residuals reached a level showing a limit-cycle behaviour. The pressure contours on the wing surface were observed. This observation and the occurrence of the limit-cycle behaviour of the residuals gave a clear indication of vortex breakdown occuring in the flow field.

The frequency spectrum associated with vortical flow containing vortex breakdown can be considered as consisting of three modes having different characteristic frequencies: the axial, the azimuthal and the radial mode. Initially, constraints on the computational resources did not allow the use of a time step to enable the resolution of the complete spectrum covering all these modes. Thus, for the time-accurate simulation, a relatively large time step was selected, aimed at a low frequency mode of approximately 1 Hz. This frequency corresponds to a self-sustained oscillation of the vortex breakdown location observed in the experiment. A non-dimensional time step $\Delta t^* = 0.1$ based on the wing chord and the free-stream velocity was determined. The free-stream state was taken as the initial state for the time-accurate simulation.

Figure 2 illustrates the time history of the surface pressure distribution. Already at time step $t^* = 0.3$, a structure consisting of primary and secondary vortices can be recognized in the surface pressure contours. The suction peak region expands until the primary vortex breaks down at $t^* = 1.3$ at a location $x/c \approx 0.6$. Immediately after the onset of breakdown, this location moves rapidly upstream until $t^* = 7.2$ reaching $x/c = 0.28$, and subsequently moves slowly downstream as the flow becomes less unsteady. Finally, the flow reaches a steady-state at $t^* = 25.6$ with the vortex breakdown location converging to a location $x/c = 0.38$.

Expecting that a smaller time step would be able to resolve unsteady phenomena, the simulation was continued (starting from the last available solution) with the non-dimensional time step equal to as small as 0.001. This continuation did not give rise to any unsteadyness. For completeness, a steady computation was performed starting with the same solution. This steady computation also did not give any indication of unsteady flow phenomena. The resulting steady-state solution is very close to the initial one, and therefore it can be interpreted as representing the asymptotic solution. It can be concluded that a large time step leads to a genuine steady-state solution of the time-dependent RANS equations. Apparently, too large a time step damps out higher frequency

modes. Indeed, during the time-accurate simulation, significant unsteadiness of high frequency components was observed in regions downstream of vortex breakdown, but the magnitude of this unsteadiness was strongly decreased in time. This confirms that the high frequency modes are responsible for the self-sustained oscillating phenomena of vortex breakdown.

In the subsequent simulation, a non-dimensional time step following a baseline (Ref. 13) $\Delta t^* = 0.0025$ is chosen, and the flow is recalculated starting from the free-stream. A self-sustained unsteady flow solution is evident after the transient appears to have decayed in $t^* = 2.25$ time steps. The simulation is performed up to $t^* = 6.5$. It is realized that the period of the lowest frequency has not yet been covered. Nevertheless, the amplitude of the high frequency mode is sustained. The instantaneous breakdown location consistently stays in the range of 67-75% chord from the apex after the onset of breakdown, in contrast to the strong shift found with the large time step of 0.1.

Figure 3 shows a power spectrum of the normal force coefficient, depicting the PSD power versus the Strouhal number resulting from the psd function of MATLAB. The figure shows a dominant peak corresponding to St $\approx 9$ ($f \approx 200$Hz). A DES computation (Ref. 13) for an isolated delta wing of the same geometry and flow condition captures a frequency of St $\approx 8$. Apart from the different flow modellings, the difference may also be attributed to the sting taken into account in the present computation.

The time-averaged surface $C_p$ contours are compared with those of the experimental results in Figure 4. In general, the pressure levels and the patterns are quite similar. A closer look is given in Figure 5 depicting $C_p$ values at the location of the pressure taps. The suction peak of the primary vortex is evident. The secondary vortices can be identified in the computational results as small suction peaks near the leading edges. Good agreement is shown up to 40% chord. Aft of this location, the computational suction peak decreases rapidly in comparison to that of the experiment. A possible explanation is that there is no local bunching of the grid within the vortex. The crossflow-plane resolution follows the leading edge sweep giving a coarsening effect significant enough to loose the physics of the vortex core. The higher pressure in the computational results in the wing centerline area can be attributed to the turbulent boundary layer.

The skin friction distribution and patterns of the limiting streamlines are shown in Figure 6, which agree well with the experimental surface oil flow patterns, showing clearly a structure containing secondary vortices.

Figures 7 and 8 show distributions of the axial velocity component of the time-averaged solution on the crossflow planes at $x/c = 0.53, 0.63, 0.74$ and $0.84$, and on a longitudinal plane along the

vortex core. Vortex breakdown occurs at $x/c \approx 0.74$, which is determined by the criterion of zero axial velocity in the vortex core. A recirculating zone downstream of the breakdown is clearly indicated. Compared to the experimental data (Figure 9), the deceleration across the breakdown is mild and the magnitude of the reversed velocity in the recirculating zone is rather small. The numerical solution gives less sharp flow feature. The streamwise grid resolution, in combination with the crossflow-plane resolution discussed above, can be made responsible for this "smeared" result. Higher grid densities should be used in the range of 60-80% chord covering the shift of breakdown location.

Figure 10 presents contours of the transversal ($v/U_o$) and normal velocity components ($w/U_o$) on the crossflow planes, respectively. The contours show gradient drops around the vortex core across the onset of vortex breakdown. The general trend is similar to the experiment, noting that the simulation gives reduced velocity magnitudes and gradients and less compact vortex. The normal and transversal locations of the vortex core, defined by the positions where there are sign reversal of the velocity components, agree with those indicated in the experiment.

Figure 11 shows the crossflow distributions of the axial component of the vorticity. Like in the experimental data, two systems can be identified having opposite signs of the vorticity. The first system contains the shear layer and the primary vortex with positive vorticity, whilst the second system contains the boundary layer and the secondary vortex with negative vorticity. The shear layer feeds vorticity into the primary vortex, while the boundary layer feeds vorticity into the secondary vortex. Across the vortex breakdown location the vorticity inside the primary vortex core is significantly dissipated. The vorticity level inside the shear layer hardly changes. Apart from the high vorticity inside the vortex (upstream of breakdown) and pockets of eddies trailing from the shear layer (Figure 12) which are not captured by the simulation, the axial vorticity levels after breakdown are roughly the same.

The azimuthal vorticity is shown in Figure 13 on the longitudinal plane along the vortex core. The colouring in the upper picture matches that shown in Figure 14 used for the experimental result. Similar but less compact flow features are revealed, while the computational vorticity level is significantly lower than that of the experiment.

Figure 15 shows the predicted turbulence kinetic energy. The turbulence intensity in the vortex is one order of magnitude less than that of the experiment. The solution features a relatively laminar vortex core, whilst there is a significant production of turbulence across the breakdown location in the vortex core. The low-turbulence vortex core is apparently a result of the modification of the turbulence model in the vortex core. This modification controls the production of the turbulence

kinetic energy through promoting the production of the dissipation rate. Although the control mechanism is dynamic in the sense that the turbulence kinetic energy is not limited to a certain level, it can be considered as too aggressive, as a reasonable agreement is still achieved in the traces of the shear layer where the control is not present.

Figure 16 presents an instantaneous and the time-averaged iso-surfaces of the total pressure loss. Two surfaces are shown, where the one with the lower value (yellow) effectively encloses that with the higher value in red. Downstream of the breakdown location, the instantaneous surface clearly indicates the spiraling characteristics stretching downstream.

## 4 Conclusions

Time-accurate simulations of a vortical flow around the ONERA 70 degree delta wing have been performed. Two non-dimensional time steps of different order of magnitude, $0.1$ and $0.0025$, have been used. The large time step has resulted in a steady-state solution containing vortex breakdown. In reaching the steady-state, high frequency components are observed in the flow field with the magnitudes rapidly decreasing in time. This confirms that a high frequency mode is responsible for the oscillating phenomena of vortex breakdown.

A physically meaningful solution has been obtained by the small time step, where a self-sustained oscillation is evident. The results have been compared with the experimental data. The characteristics across and downstream of vortex breakdown observed in the experimental data are qualitatively well reproduced by the simulation but to a lesser extent quantitatively. This may be inherent to physical modelling involved in the RANS equations. However, insufficient spatial grid resolutions, both in the crossflow planes and in the streamwise direction, may also be held responsible for the discrepancies, as suggested by a very good agreement in the pressure distribution up to 40% chord where the grid density is relatively high.

An unsteady RANS (URANS) simulation assumes a clear separation between the time scale of the main unsteady feature to be captured and the turbulence time scales. The current application lacks such a separation of scales between the unsteady vortex breakdown and the turbulence. Alternatively, one could consider the current simulation as an LES with an excessively high level of eddy viscosity, with exception of the vortex core, where the level of eddy viscosity has been effectively reduced. To improve the current results, simulations will be performed with a hybrid RANS/LES model (Ref. 7).

## 5 References

1. S. B. Anderson. Handling qualities related to stall/spin accidents of supersonic fighter aircraft. *J. Aircraft*, 22(10):875–880, 1985.

2. W. Bihrle and B. Barnhart. Departure susceptibility and uncoordinated roll-reversal boundaries for fighter configurations. *J. Aircraft*, 19(11):897–903, 1982.

3. J. W. Boerstoel, A. Kassies, J. C. Kok, and S. P. Spekreijse. *ENFLOW, A full-functionality system of CFD codes for industrial Euler/Navier-Stokes Flow Computations*. NLR TP 96286, 1996.

4. F. J. Brandsma, J. C. Kok, H. S. Dol, and A. Elsenaar. Leading edge vortex flow computations and comparison with DNW-HST wind tunnel data. RTO/AVT Vortex Flow Symposium, Loen, Norway, 2001.

5. E. F. Charlton. *Numerical stability and control analysis towards falling-leaf prediction capabilities of Splitflow for two generic high-performance aircraft models*. NASA CR-1998-208730, 1998.

6. J. C. Kok. Resolving the dependence on freestream values for the $k$-$\omega$ turbulence model. *AIAA Journal*, 38(7):1292–1294, 2000.

7. J. C. Kok, H. S. Dol, B. Oskam, and H. van der Ven. *Extra-Large Eddy Simulation of Massively Separated Flows*. NLR-TP-2003-200 (submitted for presentation at 42nd AIAA Aerospace Sciences Meeting and Exhibit, Reno, Jan. 2004), 2003.

8. J. C. Kok and S. P. Spekreijse. *Efficient and accurate implementation of the $k$-$\omega$ turbulence model in the NLR multi-block Navier-Stokes system*. NLR TP-2000-144 (presented at ECCO-MAS 2000, Barcelona, Spain, 11-14 September, 2000), 2000.

9. J. C. Kok, D. R. van der Heul, and H. S. Dol. *Predesign and results of extension of ENSOLV to weakly compressible and buoyant flow*. NLR-TR-2003-060, 2003.

10. F. H. Lutze, W. C. Durham, and W. H. Mason. Development of lateral-directional departure criteria. *AIAA Paper 93-3650*, 1993.

11. A. M. Mitchell. *Caractérisation et contrôle de l'éclatement tourbillonnaire sur une aile delta aux hautes incidences*. Ph.D dissertation, Universite Paris 6, 2000.

12. A. M. Mitchell, P. Molton, D. Barberis, and J. Délery. Characterization of vortex breakdown by flow field and surface measurements. *AIAA Paper 2000-0788*, 2000.

13. S. A. Morton, M. B. Steenman, R. M. Cummings, and J. R. Forsythe. DES grid resolution issues for vortical flows on a delta wing and an F-18C. *AIAA Paper 2003-1103*, 2003.

14. M. A. Park and L. L. Green. Steady-state computation of constant rotational rate dynamic stability derivatives. *AIAA Paper 2000-4321*, 2000.

15. B. I. Soemarwoto, O. J. Boelens, M. Allan, M. T. Arthur, K. Bütefisch, N. Ceresola, and W. Fritz. Towards the simulation of unsteady manoeuvre dominated by vortical flow. *AIAA Paper 2003-3528*, 2003.
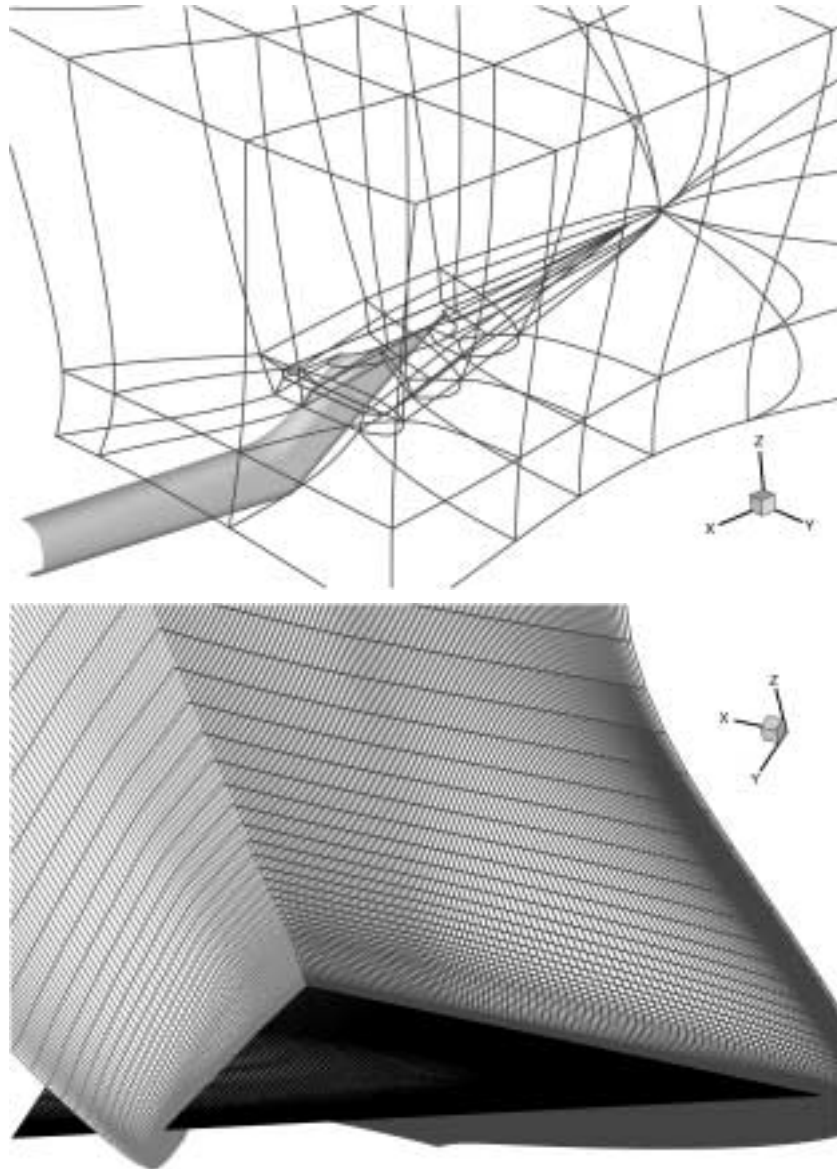
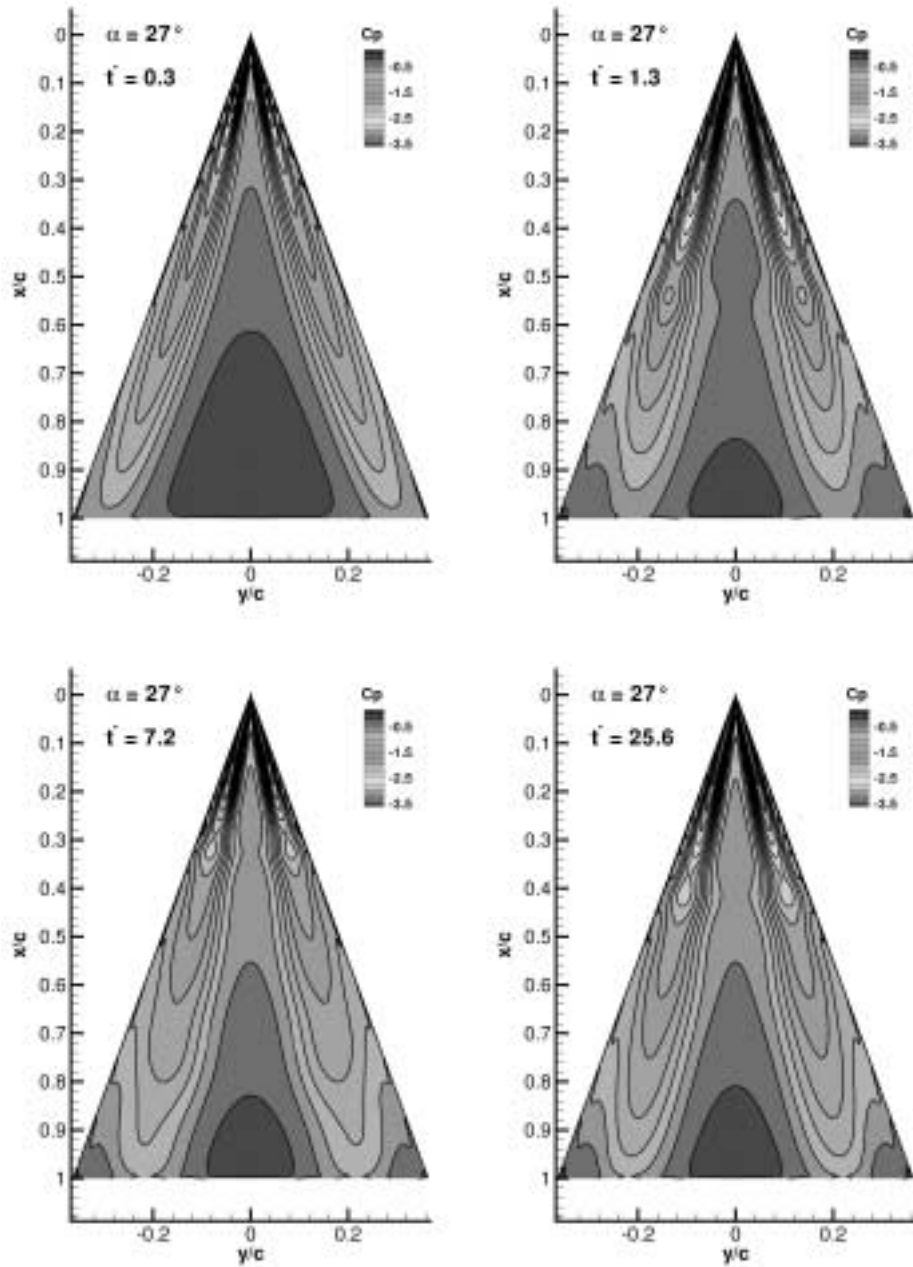*Fig. 1    Impression of the flow domain topology and computational grids.*

*Fig. 2    Computational time history of $C_p$ contours leading to a steady-state obtained with a large time step ($\Delta t^* = 0.1$).*
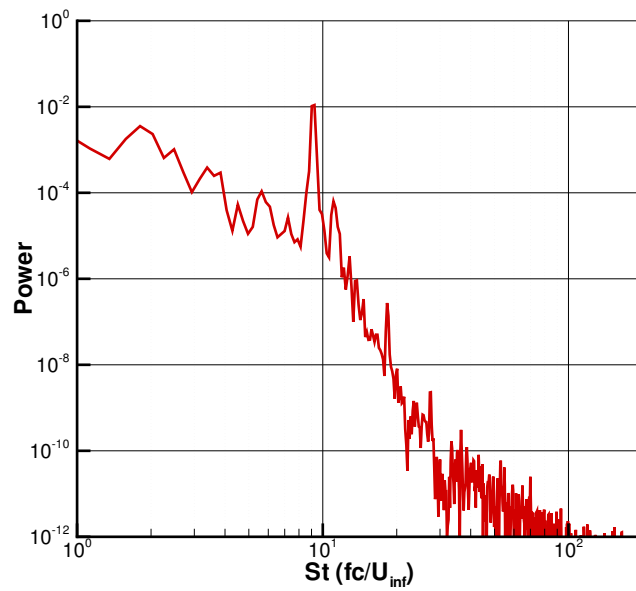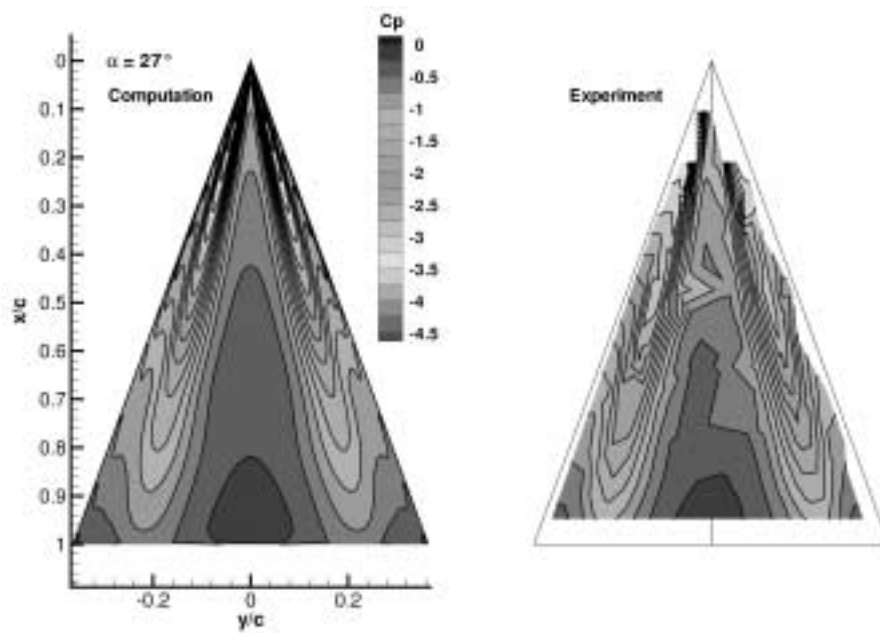
*Fig. 3    Computational power density spectra of the normal force coefficient.*



*Fig. 4    Computational and experimental time-averaged $C_p$ contours.*
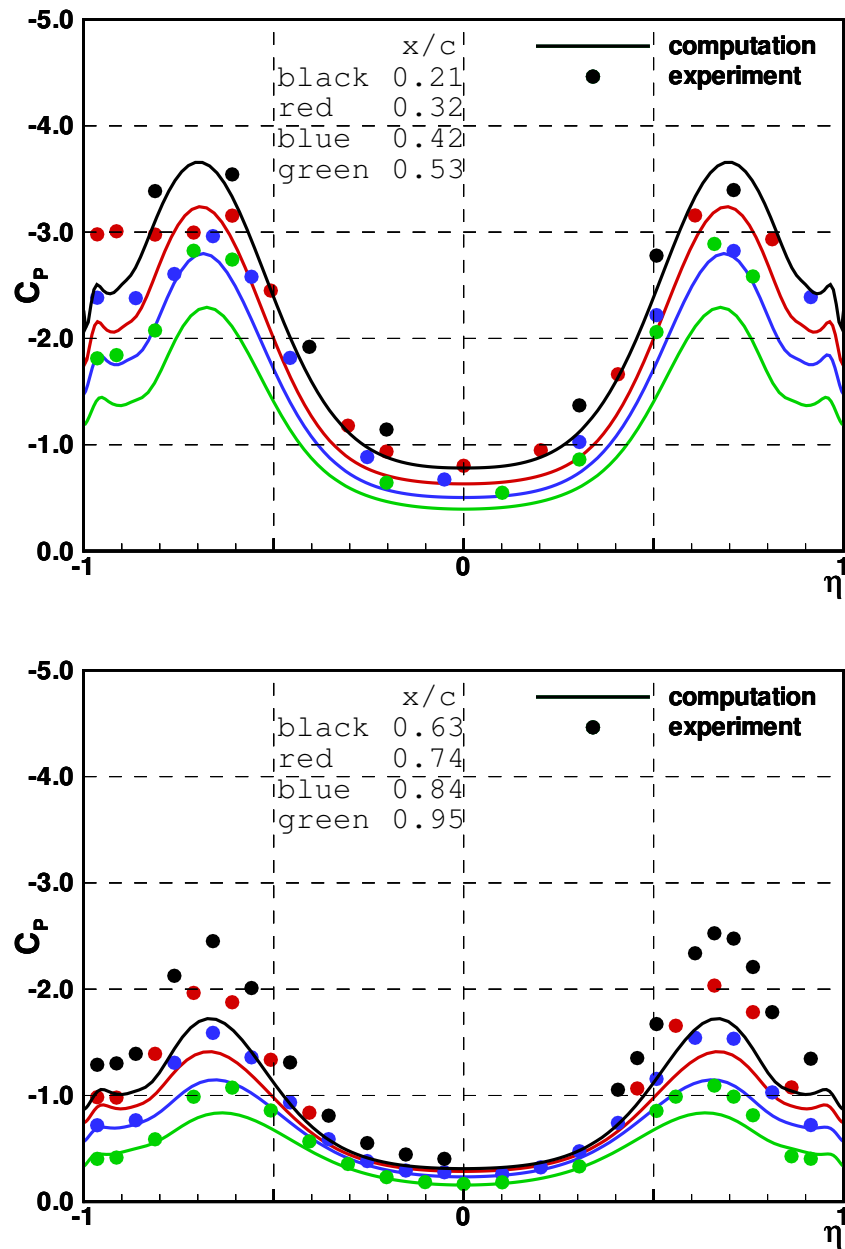
*Fig. 5    Computational and experimental spanwise $C_p$ distributions.*
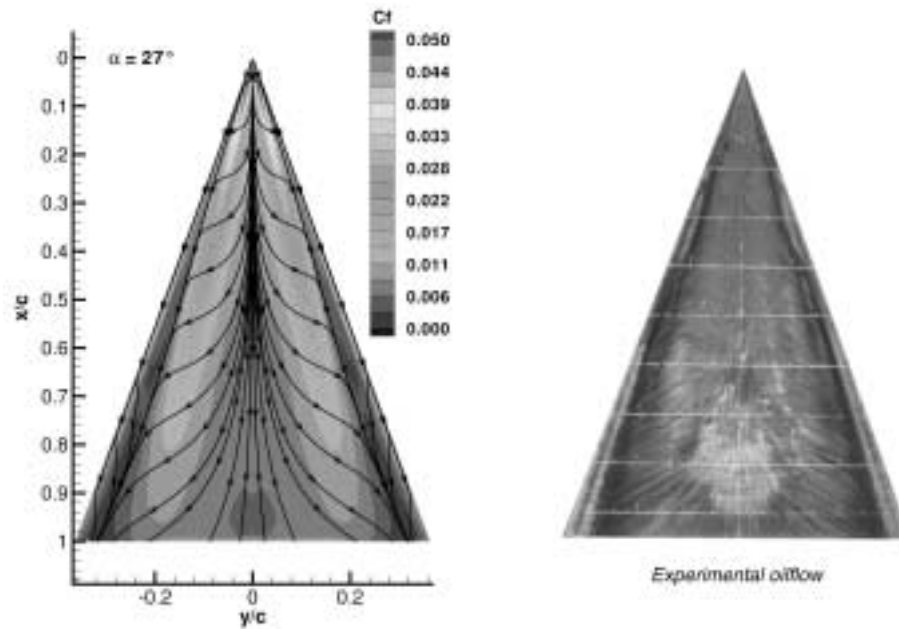
Fig. 6    Computational surface $C_f$ contours and limiting streamlines compared with the experimental oilflow pattern.
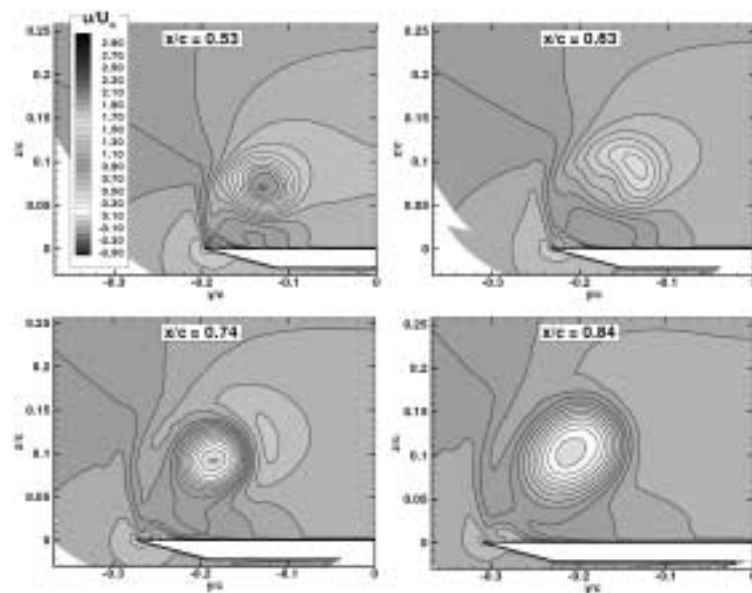


Fig. 7    Computational crossflow distribution of the axial velocity
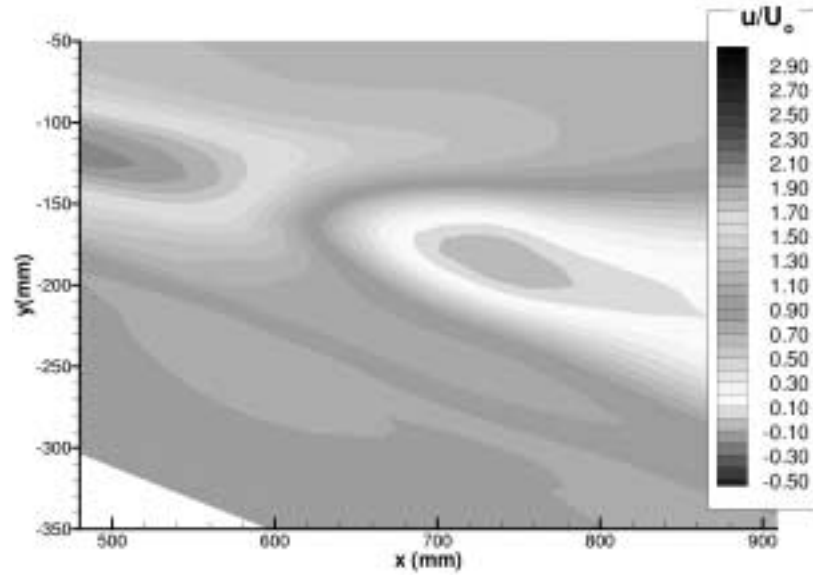
Fig. 8    Computational longitudinal distribution of the axial velocity
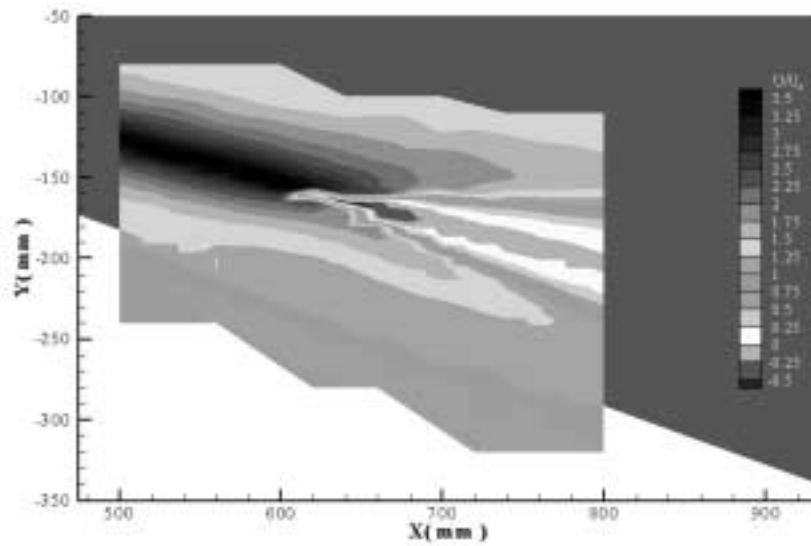


Fig. 9    Experimental longitudinal distribution of the axial velocity
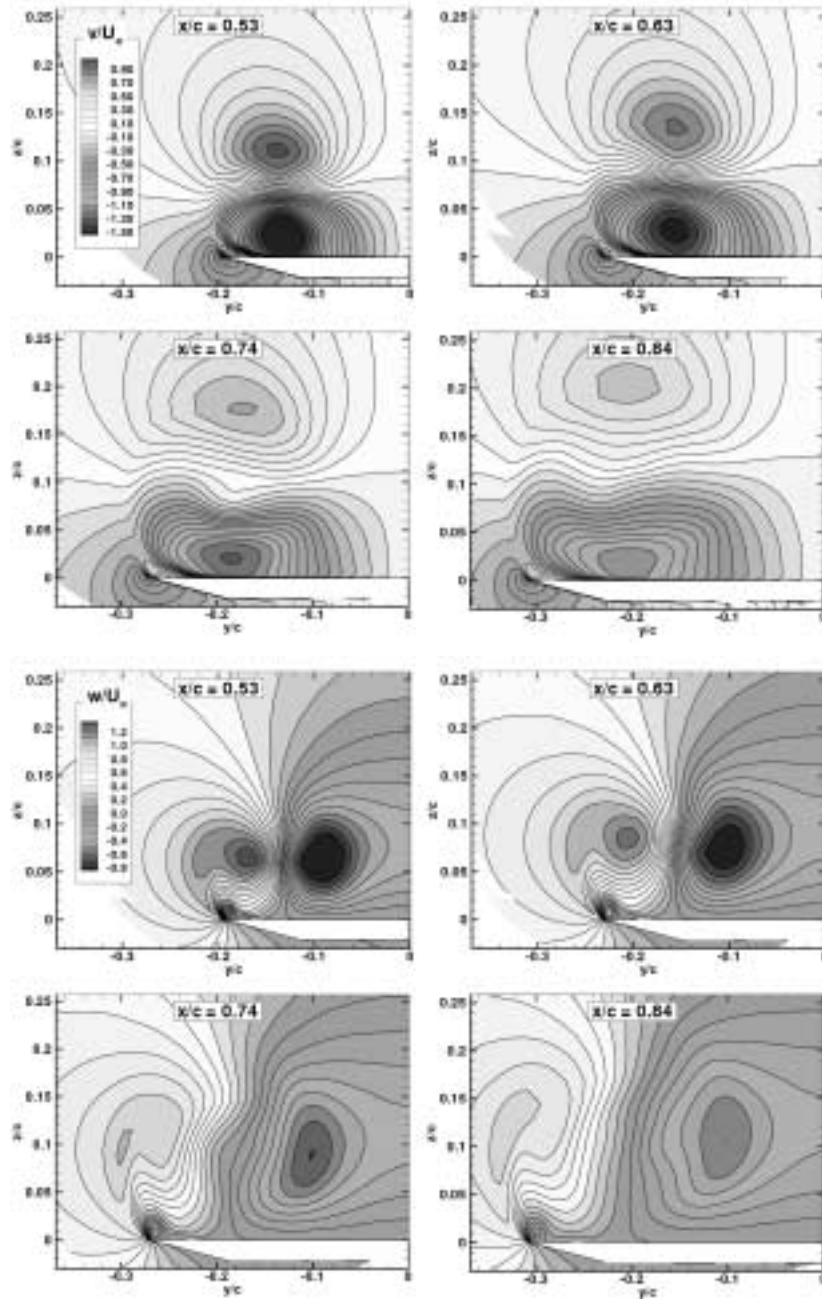
*Fig. 10    Computational crossflow distributions of the transversal ($v/U_o$ and normal ($w/U_o$) velocity.*
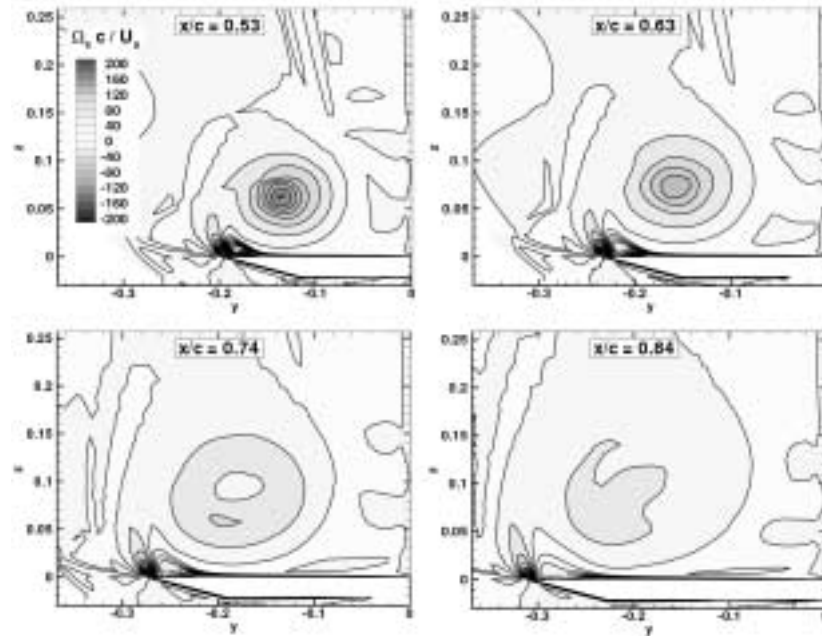
Fig. 11    Computational crossflow distributions of the axial vorticity component.
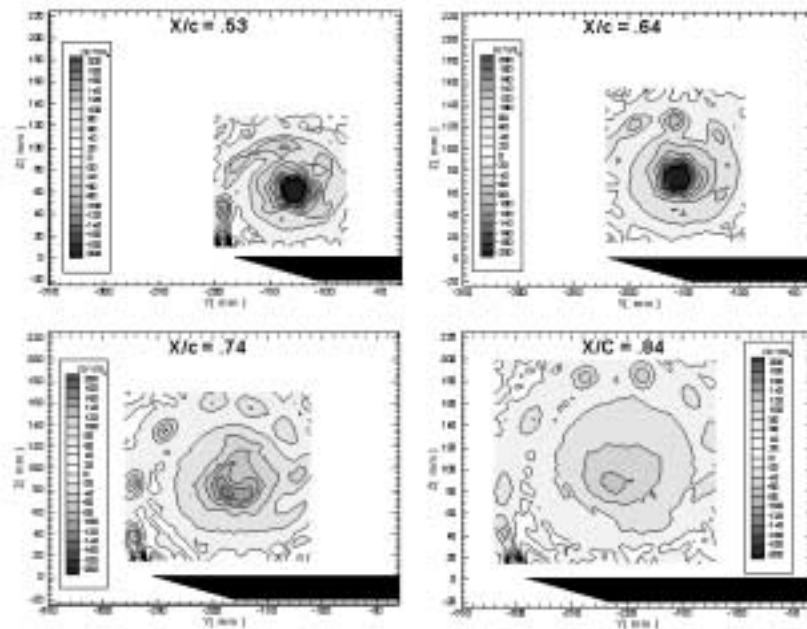


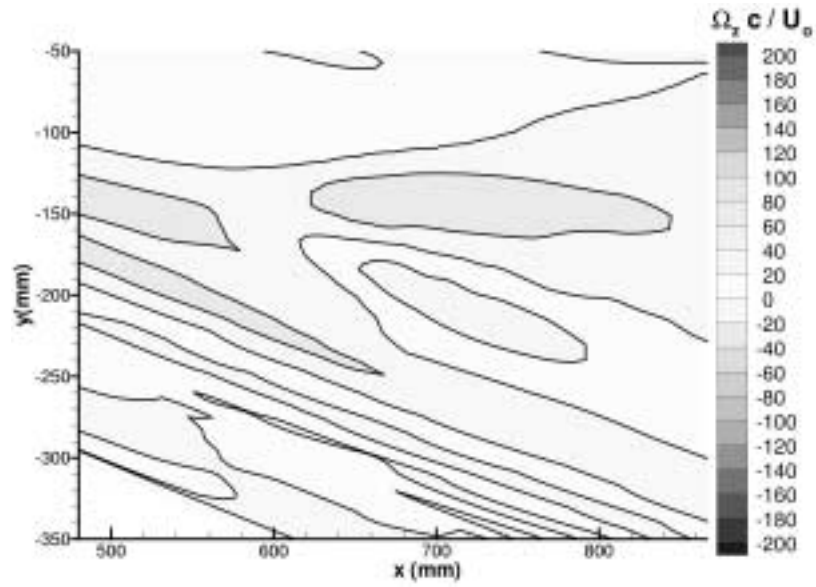Fig. 12    Experimental crossflow distributions of the axial vorticity component.

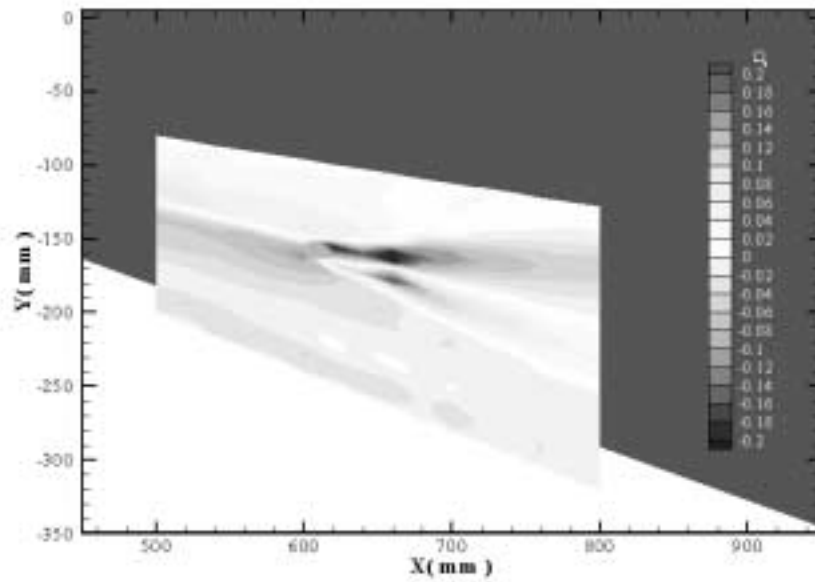Fig. 13    Computational longitudinal distribution of the azimuthal vorticity component.



Fig. 14    Experimental longitudinal distribution of the azimuthal vorticity component.
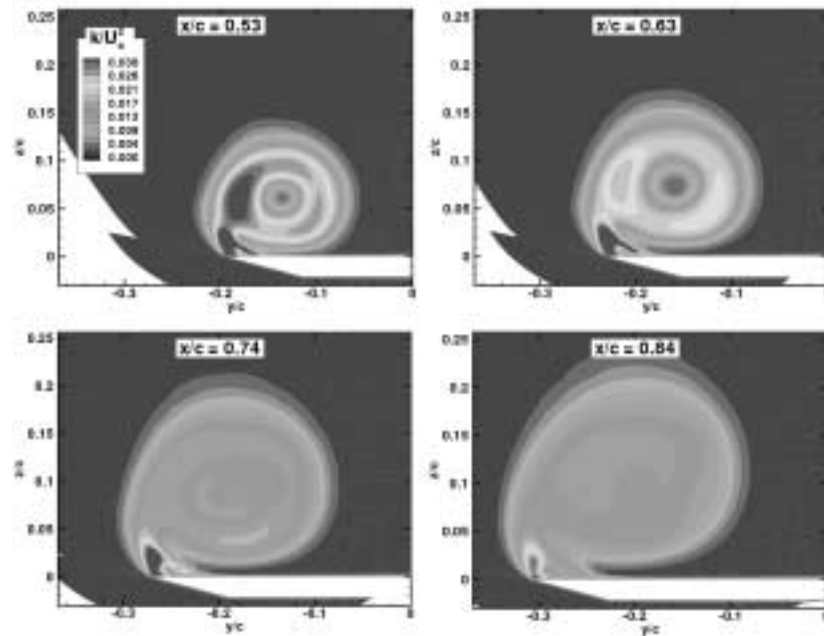
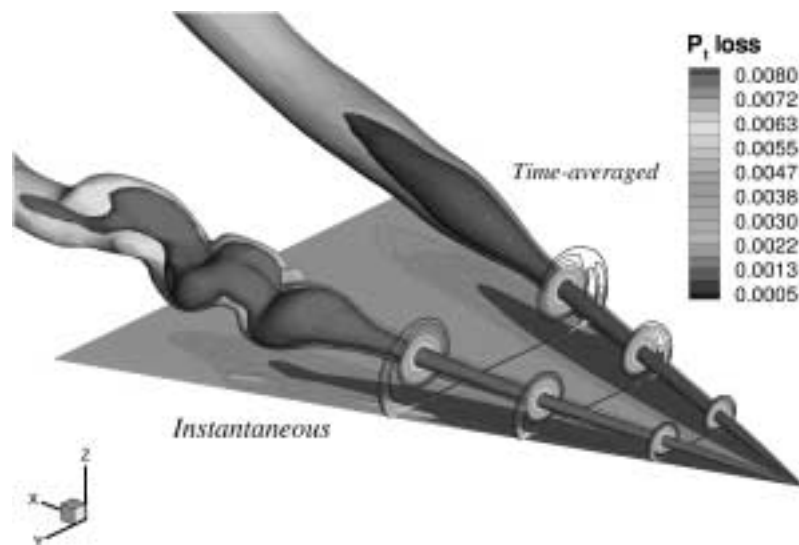Fig. 15    Computational crossflow distributions of the turbulence kinetic energy.



Fig. 16    Computational iso-surfaces of the total pressure loss.